

Breakdown of Avila’s theory in the diamond chain with quasiperiodic disorder

Manish Kumar,^{1,*} Ivan M. Khaymovich,^{2,†} and Auditya Sharma^{1,‡}

¹*Department of Physics, Indian Institute of Science Education and Research, Bhopal, Madhya Pradesh 462066, India*

²*Nordita, Stockholm University and KTH Royal Institute of Technology, SE-106 91 Stockholm, Sweden*

(Dated: March 16, 2026)

The mobility edges (MEs) that separate localized, multifractal and ergodic states in energy are a central concept in understanding Anderson localization. In this work we study the effect of several mutually commensurate quasiperiodic frequencies on the mobility edge formation. We focus on the example of the addition of a constant offset to the quasiperiodic potential of the one-dimensional all-bands-flat diamond chain. We show that this additional offset can transform the anomalous mobility edges (AMEs), i.e. the energies, separating localized and multifractal states, into conventional mobility edges, separating localized from delocalized states. Also this appears to be the first example which shows the failure of Avila’s global theory to analytically predict the ME location. We observe this violation both quantitatively, through the ME location mismatch, and qualitatively, via the formation of multiple MEs, not predicted by the theory.

I. INTRODUCTION

Anderson localization is a paradigmatic phenomenon in condensed matter physics, in which on-site disorder causes eigenstates to become localized [1]. Unlike random disorder where all states localize in one dimension in the presence of the tiniest of disorder, quasiperiodic potentials can exhibit a metal-to-insulator transition even in one dimension. The Aubry-André-Harper (AAH) model, which undergoes a transition from a fully extended phase to a fully localized phase as the strength of the quasiperiodic potential increases [2] is a prototype of this phenomenon. Furthermore, models with quasiperiodic potentials can host both localized and extended states separated by mobility edges (MEs) [3–14]. The self-duality of the standard AAH model eliminates the mobility edge, but modified versions featuring long-range hopping [7, 15–17], broken duality [9, 10, 18], diluted potentials [19, 20], or spin-orbit coupling [21, 22]—can exhibit MEs. Systems featuring MEs can show enhanced thermoelectric performance, offering promising potential for thermoelectric device applications [23–25]. The Aubry-André (AA) potential has been experimentally realized using ultracold atoms to study both single-particle [26–28] and many-body localization [29], sparking renewed interest in quasiperiodic systems at zero [30–36] and finite [37–39] temperatures.

In this work, we investigate the emergence of conventional mobility edges and anomalous mobility edges (AMEs) in a flat band [40–44] system known as the all-bands-flat (ABF) diamond chain [45], which supports compact localized states (CLS) [46, 47] as exact eigenstates in the zero disorder limit, with the spectrum given by 3 degenerate flat bands. In the presence of weak uniform random disorder, the ABF diamond chain exhibits flat band based localization that remains extremely

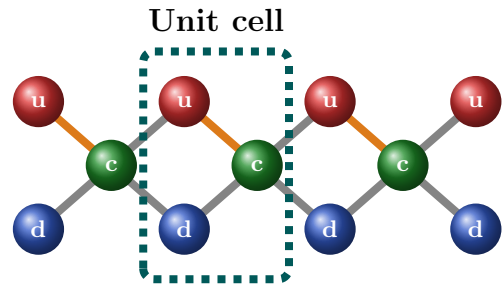


FIG. 1. Schematic of diamond lattice with u (top), c (center), and d (bottom) sites. Solid grey (orange) lines between lattice sites have the same hopping amplitude and negative (positive) sign. Dashed rectangle shows the unit cell containing three sites.

weak [45]. When this disorder is replaced by a quasiperiodic Aubry-André potential, the eigenstates become extended but non-ergodic, displaying multifractality, a subtle and increasingly studied feature of quantum systems. In the ABF diamond chain, each unit cell consists of three sites labeled by u_n (up), c_n (center), and d_n (down) as shown in Fig. 1. Interestingly, applying a symmetric quasiperiodic potential, where the same on-site potential is assigned to both the top and bottom sites of each unit cell, completely lifts the degeneracy of the flat bands while preserving the robustness of the CLS [48]. In contrast, an antisymmetric AA potential, where the on-site potentials at the top and bottom sites of each unit cell are equal in magnitude but opposite in sign and zero at the central sites, destroys both degeneracy of the flat bands and compact localization. Under such antisymmetric quasiperiodic modulation, all the states in this model are multifractal below a critical value of on-site disorder. Above this critical value AMEs, separating multifractal and localized states, emerge [49].

We introduce a constant offset $\epsilon_1 > 0$ to the Aubry-André harmonic potential of amplitude λ and apply it

* manish22@iiserb.ac.in

† ivan.khaymovich@gmail.com

‡ auditya@iiserb.ac.in

antisymmetrically across the ABF diamond chain. This modification leads to the appearance of several quasiperiodic contributions with commensurate frequencies in the effective one-dimensional Hamiltonian and, in turn, to unexpected and nontrivial changes in the nature of the eigenstates. Specifically, we observe the emergence of AMEs in the regime $\epsilon_1 < \lambda$. These AMEs originate from singularities in the transfer matrix due to vanishing effective hopping amplitudes of the above 1D Hamiltonian, accompanied by vanishingly small Lyapunov exponents (LEs) [20]. In the other limit, $\epsilon_1 > \lambda$, we find conventional MEs that separate ergodic and localized states. Thus, we present a model, having both anomalous and conventional MEs in different parameter ranges (Fig. 2), a feature not reported in earlier studies. A common diagnostic for the characterization of localization properties of eigenstates $\psi_n(E)$ is the energy E -resolved inverse participation ratio $I_q = \sum_{n=1}^N |\psi_n(E)|^{2q} \sim N^{(1-q)D_q}$, where n is a spatial index, and D_q is known as the fractal dimension. In our analysis, we use fractal dimension D_2 corresponding to $q = 2$, to characterise the localization properties of eigenstates. We further confirm these results by calculating the Lyapunov exponent γ which is positive for localized states and 0 for delocalized states.

In recent years, obtaining analytical expressions for mobility edges in various systems has received a great deal of interest. A major breakthrough in this direction has been the use of Avila's global theory [50], one of the seminal contributions that earned him the Fields Medal. This theory has since been applied widely, and its predictions have been verified numerically across multiple models [19, 51–54]. In the case of the ABF diamond chain with the AA potential but without any constant offset, the analytical expression for the ME ($|E| = 4/\lambda$) has already been obtained [49, 55] using insights from the extended Harper model [56]. In this work, we apply Avila's global theory to the ABF diamond chain with both the AA potential and a constant offset $\epsilon_1 \geq 0$. The expression obtained from Avila's theory agrees with the extended Harper model result when $\epsilon_1 = 0$. However, for $\epsilon_1 > 0$, the analytical prediction from Avila's global theory remains only qualitatively valid for $\lambda \gtrsim 2$ and fails quantitatively. To achieve quantitative agreement, we introduce fitting parameters into the analytical formula and verify the modified expression through careful numerical analysis for several values of $\lambda \gtrsim 2$. Furthermore, we demonstrate that for $\lambda \lesssim 2$, Avila's theory breaks down even qualitatively due to the presence of multiple mobility edges which are not predicted by the above theory.

The paper is organized as follows: In Section II we introduce the model. In Section III we show the analytical derivation of the ME expression using Avila's theory. Section IV is devoted to multifractal analysis to determine ME locations numerically. We confirm the results by calculating the Lyapunov exponent and the power-law decay exponent in Sec. V. Finally, we discuss the disagreement of our results with Avila's global theory

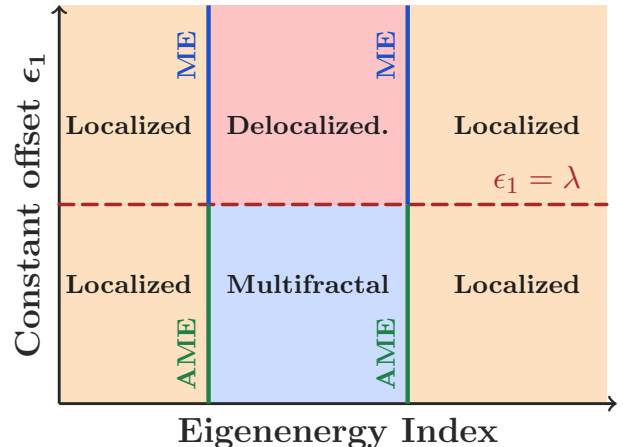


FIG. 2. A schematic showing the presence of AMEs in $\epsilon_1 < \lambda$ regime and MEs in $\epsilon_1 > \lambda$ regime.

in section VI. The results are summarized in Sec. VII. An additional phase diagram for $\lambda = 0.8$ is provided in Appendix A. Numerical results are supported by Lyapunov exponent analysis in Appendix B. Appendix C demonstrates the emergence of multiple anomalous mobility edges at higher potential strength. We further confirm our results with I_2 collapse analysis in Appendix D. Finally, Appendix E presents results for a single realization of the phase parameter θ .

II. MODEL

We consider a single-particle model on a quasi-one-dimensional diamond lattice (see Fig. 1), whose Hamiltonian is given by [45, 49]:

$$\hat{H} = \hat{H}_{\text{hop}} + \hat{H}_{\text{os}}, \quad (1)$$

where

$$\begin{aligned} \hat{H}_{\text{hop}} &= -J \sum_{n=1}^{N/3} \left(-\hat{u}_n^\dagger \hat{c}_n + \hat{c}_n^\dagger \hat{d}_n + \hat{c}_n^\dagger \hat{u}_{n+1} + \hat{c}_n^\dagger \hat{d}_{n+1} \right) + \text{H.c.}, \\ \hat{H}_{\text{os}} &= \sum_{n=1}^{N/3} \left(\zeta_n^u \hat{u}_n^\dagger \hat{u}_n + \zeta_n^c \hat{c}_n^\dagger \hat{c}_n + \zeta_n^d \hat{d}_n^\dagger \hat{d}_n \right). \end{aligned} \quad (2)$$

Here, each unit cell n consists of three sites, hence the total number of sites denoted by $N = 3L$ should be a multiple of 3. \hat{u}_n^\dagger , \hat{c}_n^\dagger , and \hat{d}_n^\dagger are fermionic creation operators acting at the u (up), c (center), and d (down) sites respectively in the n^{th} unit cell as shown in the schematic (Fig. 1). J is the nearest neighbor hopping amplitude, which we choose to be $J = 1$ without loss of generality. ζ_n^α ($\alpha = \text{u, c, d}$) denotes on-site potential on the n^{th} site. The on-site energies are drawn from a quasiperiodic

antisymmetric potential according to:

$$\zeta_n^c = 0, \quad \zeta_n^u = -\zeta_n^d = \epsilon_1 + \lambda \cos[2\pi\beta n + \theta] \quad (3)$$

where ϵ_1 is an offset potential, and λ is the potential strength. The quasiperiodicity parameter β is an irrational number to ensure the incommensurate nature of the potential. In order to implement periodic boundary conditions, we take the number of unit cells to be $L = F_l$ (Fibonacci number l), and adopt a rational approximant $\beta_l \equiv F_{l-1}/F_l$ of $\beta = \lim_{l \rightarrow \infty} \beta_l$. In the limit $l \rightarrow \infty$, this ratio converges to an irrational number, thereby preserving quasiperiodicity. θ is chosen randomly from a uniform distribution between $[0, 2\pi]$. Unless explicitly stated otherwise, all quantities are averaged over 50 realizations of θ .

In the absence of disorder ($\zeta_n^c = 0$), the diamond chain exhibits three flat bands at energies $\pm 2, 0$ and for this reason this system is also known as the all-bands-flat diamond chain. Also, this system possesses only compactly localized states. Hence, one can conclude that in the zero disorder limit, the system is highly degenerate, a good insulator and possesses chiral symmetry. If we put a symmetric potential, where the same potential is applied to the top and bottom sites of a unit cell, $\zeta_n^u = \zeta_n^d$, compact localization is preserved although degeneracy is lifted. In this work we consider the quasiperiodic potential applied in an antisymmetric manner (see (3)). For $\epsilon_1 = 0$, this model reduces to the case which has been already studied. In the antisymmetric case, not only is the degeneracy lifted but the compact localization of eigenstates is also destroyed. In the low disorder regime, all the eigenstates are extended but non-ergodic while with increasing disorder strength λ , anomalous mobility edges, which separate localized and multifractal states, are observed [49].

III. AVILA'S GLOBAL THEORY

In this section, we demonstrate how an analytical derivation of the MEs may be obtained using Avila's theory [50]. We start by computing the transfer matrix of our system. To write the transfer matrix, we first write the lattice equation of the effective 1D model of the diamond chain. Starting from the Schrödinger equation of the Hamiltonian in the site basis, we obtain the following set of coupled equations for the components u_k, d_k , and c_k of the wavefunction $\psi_k(E) = (u_k, d_k, c_k)^T$ in the k -th unit cell:

$$\begin{aligned} Eu_k &= \zeta_k u_k + Jc_k - Jc_{k-1}, \\ Ec_k &= Ju_k - Jd_k - Ju_{k+1} - Jd_{k+1}, \\ Ed_k &= -\zeta_k d_k - Jc_k - Jc_{k-1}. \end{aligned} \quad (4)$$

To simplify the structure of the equations, we perform the unitary transformation

$$\begin{aligned} p_k &= \frac{u_k - d_k}{2} + \frac{c_k}{\sqrt{2}}, \\ q_k &= -\frac{u_k - d_k}{2} + \frac{c_k}{\sqrt{2}}, \\ s_k &= \frac{u_k + d_k}{\sqrt{2}}, \end{aligned} \quad (5)$$

which diagonalizes the intracell hopping matrix and renders the antisymmetric structure explicit. In the case of antisymmetric on-site disorder the Schrödinger equation in the rotated basis (u_k, d_k, c_k) takes the form

$$Ep_k = \frac{\zeta_k}{\sqrt{2}} s_k - (-\sqrt{2}p_k + s_{k+1}), \quad (6)$$

$$Eq_k = -\frac{\zeta_k}{\sqrt{2}} s_k - (\sqrt{2}q_k + s_{k+1}), \quad (7)$$

$$Es_k = \frac{\zeta_k}{\sqrt{2}} (p_k - q_k) - (p_{k-1} + q_{k-1}). \quad (8)$$

Substituting the expressions for p_k and q_k from the first two equations into the third expression, we obtain the lattice equation for the diamond chain in the case of antisymmetric on-site disorder:

$$E[E^2 - 4]s_k = \zeta_k^2 Es_k - 2\zeta_k s_{k+1} - 2\zeta_{k-1} s_{k-1}, \quad (9)$$

with the effective energy $E(E^2 - 4)$, quasiperiodic E -dependent effective on-site potential $\zeta_k^2 E$ with a period π/β , and the quasiperiodically modulated hopping $2\zeta_k$, with another period $2\pi/\beta$. One can write this equation in terms of the transfer matrix also as

$$\psi_{k+1} = T_k \psi_k \quad (10)$$

where $\psi_k^T = (s_k \ s_{k-1})^T$. T_k is the transfer matrix:

$$T_k(\theta) = \begin{pmatrix} \frac{E}{2} \left[\zeta_k - \frac{E^2-4}{\zeta_k} \right] & -\frac{\zeta_{k-1}}{\zeta_k} \\ 1 & 0 \end{pmatrix} \quad (11)$$

with $\zeta_k = \epsilon_1 + \lambda \cos[2\pi k\beta + \theta]$. The next step is to calculate the Lyapunov exponent which is related to localization length. The Lyapunov exponent is inversely related to the localization length, hence, for an extended eigenstate it decreases with increasing system size and tends to zero in the thermodynamic limit. In contrast, localized states are characterized by a finite LE. The transfer matrix can be used to calculate the LE:

$$\gamma(E) = \lim_{L \rightarrow \infty} \frac{1}{L} \ln \frac{|\psi_L|}{|\psi_0|}, \quad (12)$$

where L is the number of unit cells. The wavefunction can be written as

$$\psi_L = T_L T_{L-1} \cdots T_2 T_1 \psi_0 \quad (13)$$

where T_L is the transfer matrix. Putting it in $\gamma(E)$, we get

$$\gamma(E) = \lim_{L \rightarrow \infty} \frac{1}{L} \ln \frac{|T_L T_{L-1} \cdots T_2 T_1 \psi_0|}{|\psi_0|}. \quad (14)$$

For almost any choice of ψ_0 , the growth rate of ψ_i is governed by the same Lyapunov exponent [57]. This leads to the simplification:

$$\begin{aligned} \gamma(E) &= \lim_{L \rightarrow \infty} \frac{1}{L} \ln \|T_L T_{L-1} \cdots T_1\| \\ &= \lim_{L \rightarrow \infty} \frac{1}{L} \ln \left\| \prod_{k=1}^L T_k \right\|. \end{aligned} \quad (15)$$

In the transfer matrix (11), we can't use Avila's theory directly as ζ_k has incommensurately distributed zeros. So we first pull out the singularity as a factor by writing [58]:

$$\begin{aligned} T_k(\theta) &= \frac{1}{2\zeta_k} \begin{pmatrix} E[\zeta_k^2 - E^2 + 4] & -2\zeta_{k-1} \\ 2\zeta_k & 0 \end{pmatrix} \\ &= A_k B_k \end{aligned} \quad (16)$$

where

$$A_k(\theta) = \frac{1}{2\zeta_k}, \quad B_k(\theta) = \begin{pmatrix} E[\zeta_k^2 - E^2 + 4] & -2\zeta_{k-1} \\ 2\zeta_k & 0 \end{pmatrix}. \quad (17)$$

Since $T_k(\theta)$ is decomposed into two parts as in Eq. (17), the total LE is $\gamma(E) = \gamma^A(E) + \gamma^B(E)$ where we focus separately on both summands. For $\gamma^A(E)$ we have

$$\begin{aligned} \gamma^A(E) &= \lim_{L \rightarrow \infty} \frac{1}{L} \ln \left\| \prod_{k=1}^L A_k(\theta) \right\| \\ &= \lim_{L \rightarrow \infty} \frac{1}{L} \ln \left\| \prod_{k=1}^L \frac{1}{2(\epsilon_1 + \lambda \cos[2\pi k\beta + \theta])} \right\|. \end{aligned}$$

We consider the complex extension of LE, denoted by $\gamma_\epsilon^A(E)$, by complexifying the phase, i.e. $\theta \rightarrow \theta + i\epsilon$,

$$\gamma_\epsilon^A(E) = \lim_{L \rightarrow \infty} \frac{1}{L} \ln \left\| \prod_{k=1}^L \frac{1}{2(\epsilon_1 + \lambda \cos[2\pi k\beta + \theta + i\epsilon])} \right\|. \quad (18)$$

Since β is an irrational number, as k varies, the argument of the cosine fills the interval $(0, 2\pi)$ uniformly. This follows from Weyl's equidistribution theorem and properties of irrational rotations [59, 60]. Then by using the classical Jensen's formula [61, 62] and ergodic theory, we can write

$$\begin{aligned} \gamma^A(E) &= \frac{1}{2\pi} \int_0^{2\pi} \ln \frac{1}{2(\epsilon_1 + \lambda \cos(\theta + i\epsilon))} d\theta \\ &= \begin{cases} \ln \frac{1}{\lambda} - \epsilon & \text{if } \epsilon_1 < \lambda \\ \ln \frac{1}{\epsilon_1 + \sqrt{\epsilon_1^2 - \lambda^2}} & \text{if } \epsilon_1 > \lambda \end{cases}. \end{aligned} \quad (19)$$

Here in $\epsilon_1 < \lambda$ regime, we have to work with the multi-valued complex logarithm function; we choose the branch such that the Lyapunov exponent remains real and continuous at $\epsilon = 0$. With this choice we obtain the λ -independent term to be $-\epsilon$. We use Avila's global theory [50] to calculate γ^B [54] as

$$\gamma_\epsilon^B(E) = \lim_{L \rightarrow \infty} \frac{1}{2\pi L} \int_0^{2\pi} \ln \|B_k(\theta)\| d\theta. \quad (20)$$

According to Refs. [53, 56, 63], the presence ($\epsilon_1 < \lambda$) [absence ($\epsilon_1 > \lambda$)] of a singularity in the transfer matrix, Eq. (11), excludes (allows) the existence of the ergodic states in the spectrum. Thus, only AMEs are realized for $\epsilon_1 < \lambda$, while only the conventional MEs appears for $\epsilon_1 > \lambda$. Using Eq. (17), the characteristic equation of B_k is $X^2 - \text{tr}(B_k)X + \det(B_k) = 0$, where X are eigenvalues of B_k . On solving,

$$X = \frac{(E\zeta_k^2 - E^3 + 4E) \pm \sqrt{(E\zeta_k^2 - E^3 + 4E)^2 - 16\zeta_k\zeta_{k-1}}}{2}. \quad (21)$$

ζ_k depends on θ so we first complexify the phase, i.e. $\theta \rightarrow \theta + i\epsilon$, and take $\epsilon \rightarrow \infty$. Then ζ_k becomes

$$\zeta_k \approx \frac{\lambda}{2} e^\epsilon e^{-i\phi}$$

with $\phi = 2\pi k\beta + \theta$ and the largest eigenvalue of B_k is

$$X \approx \frac{E\lambda^2}{4} e^{2\epsilon} e^{-2i\phi} + O(1).$$

The norm of B_k is $\|B_k\| = e^{2\epsilon} \frac{E\lambda^2}{4} + O(1)$. Note that it is independent of k , hence $\|B_k(\theta)\| = \left\| \prod_{k=1}^L B_k \right\| = \|B_k\|^L$.

Again using the classical Jensen formula and ergodic theory, we can write

$$\begin{aligned} \gamma_\epsilon^B(E) &= \lim_{L \rightarrow \infty} \frac{1}{2\pi L} \int_0^{2\pi} \ln \|B_k\|^L d\theta \\ &= 2\epsilon + \ln \left| \frac{E\lambda^2}{4} \right| + O(e^{-4\pi\epsilon}). \end{aligned} \quad (22)$$

This is the expression of γ_ϵ^B as $\epsilon \rightarrow \infty$. Using Eq. (19) and (22), the total LE can be written as:

$$\gamma_\epsilon(E) = \begin{cases} \epsilon + \ln \left| \frac{E\lambda}{4} \right| + O(e^{-4\pi\epsilon}), & \epsilon_1 < \lambda \\ 2\epsilon + \ln \left| \frac{E\lambda^2}{4\epsilon_1 + 4\sqrt{\epsilon_1^2 - \lambda^2}} \right| + O(e^{-4\pi\epsilon}), & \epsilon_1 > \lambda \end{cases}. \quad (23)$$

To calculate the localization length we are interested in the minimum Lyapunov exponent, i.e. γ_0 . Avila's global theory of one frequency analytical $SL(2, \mathbb{R})$ cocycle, shows that γ_ϵ is a convex, piecewise linear function of ϵ with slope defined as:

$$\omega(E) = \lim_{\epsilon \rightarrow 0^+} \frac{\gamma_\epsilon(E) - \gamma_0(E)}{\epsilon}, \quad (24)$$

being quantized. As we can see from Eq. (23), the slope $\omega(E)$ of $\gamma_\epsilon(E)$ with respect to ϵ , is 2 for $\epsilon_1 > \lambda$ and 1 for $\epsilon_1 < \lambda$ as $\epsilon \rightarrow \infty$. Since $\omega(E)$ is quantized, as we start decreasing ϵ from ∞ , the slope in the neighborhood of $\epsilon = 0$ can be 2, 1 or 0 in $\epsilon_1 > \lambda$ regime and 1 or 0 in $\epsilon_1 < \lambda$ regime. Moreover, by Avila's global theory, the energy does not belong to the spectrum, iff $\gamma_0(E) > 0$ and $\gamma_\epsilon(E)$ is flat in the neighborhood of $\epsilon = 0$. Using these conclusions from Avila's global theory, the spectrum can be decomposed into three parts as can be seen in Table I. Consequently, for the case where E belongs

$\gamma_{\epsilon=0}$	$\omega _{\epsilon=0}$	State behavior
> 0	$= 0$	$E \notin \Sigma$
> 0	> 0	Localized
$= 0$	> 0	Critical
$= 0$	$= 0$	Ergodic

TABLE I. Classification of states based on γ_ϵ and ω

to the spectrum we can write:

$$\gamma_\epsilon(E) = \begin{cases} \max \left[\ln \left| \frac{E\lambda}{4} \right|, 0 \right], & \epsilon_1 < \lambda \\ \max \left[\ln \left| \frac{E\lambda^2}{4\epsilon_1 + 4\sqrt{\epsilon_1^2 - \lambda^2}} \right|, 0 \right], & \epsilon_1 > \lambda \end{cases} \quad (25)$$

Then the mobility edge can be determined by $\gamma(E) = 0$, which gives

$$|E| = \begin{cases} \frac{4}{\lambda} & \text{if } \epsilon_1 < \lambda \\ \frac{4(\epsilon_1 + \sqrt{\epsilon_1^2 - \lambda^2})}{\lambda^2} & \text{if } \epsilon_1 > \lambda \end{cases} \quad (26)$$

The expression for $\epsilon_1 = 0$ exactly matches the form of the MEs previously obtained for the ABF diamond chain with only the AA potential [49], which was derived using an analogy with the extended Harper model [56]. However, for $\epsilon_1 > 0$, our analytical expression does not fully agree with the numerical results. For $\epsilon_1 > \lambda$, the discrepancy arises because, within Avila's approximation, the expression obtained for γ_ϵ^B [Eq. (22)] exhibits a slope of 2 as $\epsilon \rightarrow \infty$. According to Avila's theory, in the neighborhood of this regime, the Lyapunov exponent can only have slopes of 2, 1, or 0. Therefore, the MEs given by Eq. (26) effectively separate the states corresponding to slope 2 from those with slopes 1 and 0. On the other hand, for $\epsilon_1 < \lambda$ regime the discrepancy between analytical and numerical results arises even when γ_ϵ^B [Eq. (22)] exhibits a slope of 1. This deviation may be attributed to the massive degeneracy inherent to the ABF diamond chain, where for $\epsilon_1 < \lambda$ the energy levels remain strongly clustered, potentially modifying the spectral structure beyond the assumptions underlying the analytical approximations in Avila's global theory.

To the best of our knowledge, our work is the first to report the emergence of such a slope-2 behavior in

this context, suggesting a possible breakdown or limitation of Avila's theoretical framework when applied to the diamond-chain lattice with antisymmetric disorder. Nonetheless, we find that the MEs obtained by fitting Eq. (31) for $\epsilon_1 > \lambda$ remain consistent with the numerical data in the large λ limit. We will explain this fitting protocol later in this paper. Moreover, as we will see below, the overall picture of the AMEs for $\epsilon_1 < \lambda$, transforming into the conventional one for $\epsilon_1 > \lambda$ is consistent with the singular/regular properties of the transfer matrix, mentioned in [56, 58, 63].

IV. FRACTAL DIMENSION ANALYSIS

To verify the analytically derived mobility edges from Avila's theory, we perform a numerical analysis based on the fractal characteristics of the eigenstates. In this study, we focus on the regime with $\epsilon_1 > 0$. A standard tool for probing the localization properties of wave functions is the inverse participation ratio (I_2), which quantifies the extent of localization. The IPR for a given eigenstate is defined as

$$I_q = \sum_{n=1}^L \sum_{\alpha=u,c,d} |\alpha_n(E)|^{2q} \quad (27)$$

where $\alpha_n(E)$ denotes the probability amplitude of the eigenstate with energy E at the $\alpha = u, c, d$ site of the n -th unit cell, i.e., $\alpha_n(E) \in \{u_n(E), c_n(E), d_n(E)\}$ from Eq. (2). The corresponding basis states $|\alpha_n\rangle$ represent single particle states localized at site α in the n -th unit cell. IPR scales with system size N as $N^{-1}(N^0)$ for delocalized (localized) states. A more complete study of localization can be done using fractal dimension D_q . In our analysis we focus on fractal dimension D_2 , corresponding to $q = 2$, which is given by $D_2 = -\lim_{N \rightarrow \infty} \frac{\ln(I_2)}{\ln N}$. It is known that $D_2 \rightarrow 1$ for extended states, $D_2 \rightarrow 0$ for localized states and D_2 lies between 0 and 1 for multifractal states. Fig. 3(a)-(c) shows the energy-resolved θ -averaged D_2 as a function of shift in potential ϵ_1 for the entire spectrum for potential strength $\lambda = 10$, $\lambda = 5$, and $\lambda = 2$, respectively. Green dashed lines are mobility edges obtained using Avila's theory given by Eq. (26). The ergodic-localized (MEs) and multifractal-localized anomalous mobility edges (AMEs) can be observed for $\epsilon_1 > \lambda$ and $\epsilon_1 < \lambda$, respectively in full agreement with [56, 58, 63]. The emergence of multifractal states in the regime $\epsilon_1 < \lambda$ is due to singularities in the transfer matrix T_k , which arise when the quasiperiodic coefficient ζ_k vanishes. Since ζ_k appears in the denominator of the matrix elements, its zeros lead to singular behavior of the transfer matrix at specific lattice sites.¹ In the ther-

¹ This mechanism of small (evenly distributed) zeros in the hopping terms, present, e.g., in uncorrelated Anderson models on

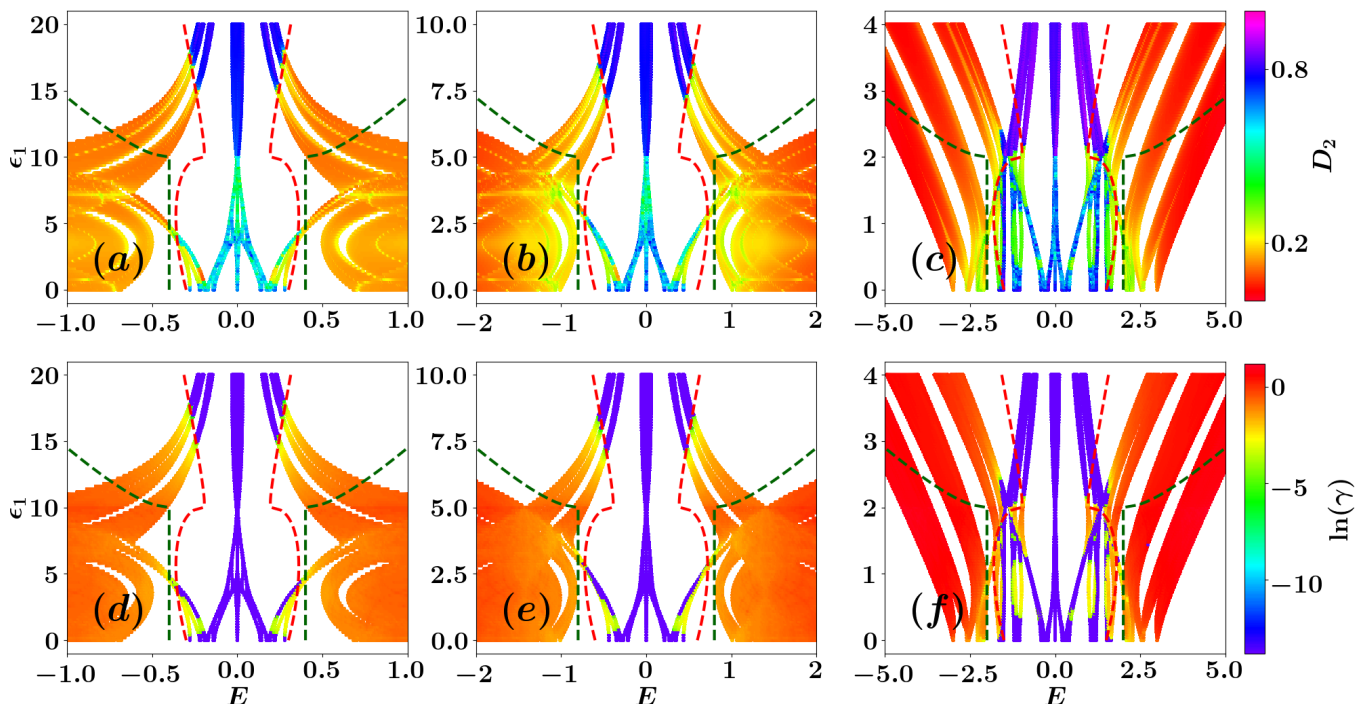


FIG. 3. (a)-(c) The fractal dimension D_2 (whose magnitude is captured as shown in the colorbar) as a function of increasing ϵ_1 and energy E for (a) $\lambda = 10$, (b) $\lambda = 5$, and (c) $\lambda = 2$. (d)-(f) The Lyapunov exponent γ (whose magnitude in the logscale is captured as shown in the colorbar) as a function of increasing ϵ_1 and energy E for (d) $\lambda = 10$, (e) $\lambda = 5$, and (f) $\lambda = 2$. Here averaging is done over 50 values of θ . The system size is $N = 12543$ and $J = 1$. Green dashed lines are Avila's theory predictions given by Eq. (26) and red dashed lines correspond to the modified analytical expression using fitting, given by Eq. (31).

modynamic limit, these zeros are distributed in an incommensurate manner, affecting the spatial structure of the eigenstates. As a result, the system cannot support fully extended states in this regime. Instead, depending on the Lyapunov exponent, the spectrum consists of either localized states with finite Lyapunov exponent or critical (multifractal) states characterized by vanishing Lyapunov exponent. Our results confirm the presence of AMEs in the $\epsilon_1 < \lambda$ regime. In contrast, for $\epsilon_1 > \lambda$, ζ_k does not vanish and the transfer matrix remains regular hence the ergodic states are allowed and we observe conventional MEs separating localized from extended states.

Another noteworthy observation is the apparent violation of Avila's global theory as shown in Fig. 3(a)-(c), where green dashed lines correspond to Avila's theory predictions given by Eq. (26). Reddish regions, indicating localized states, appear between the analytical MEs in the $\epsilon_1 > \lambda$ regime. Similarly, yellowish and greenish regions observed for $\epsilon_1 < \lambda$ also suggest localized behavior between analytical AMEs. For $\lambda = 0.8$, as shown in Appendix A, the disagreement with Avila's theory is even stronger. These results indicate that Avila's formal-

ism deviates quantitatively and does not perfectly separate localized states from ergodic and multifractal ones. We confirm this conclusion through Lyapunov exponent analysis in the following section.

V. LYAPUNOV EXPONENT ANALYSIS

To further validate the results obtained from the fractal dimension analysis, we numerically examine the Lyapunov exponent (LE). The LE, denoted by $\gamma(E)$, quantifies the exponential rate at which a wave function localizes around the location of its maximum n_0 . For a localized state, the probability density decays as

$$|\psi_n(E)|^2 \sim \exp[-2\gamma(E)|n - n_0|], \quad (28)$$

where a finite $\gamma(E) > 0$ indicates exponential localization. In contrast, $\gamma(E) = 0$ corresponds to delocalized states, as observed in ergodic extended phases. We compute $\gamma(E)$ for all eigenstates by fitting their spatial wave function profiles using Eq. (28). Numerically, both delocalized and multifractal states yield $\gamma \approx 0$.

To ensure the robustness of fitting, we evaluate the goodness of fit parameter R^2 for each eigenstate. For localized states the fits are robust with $R^2 \approx 1$. However in the multifractal and delocalized regimes, the wavefunc-

hierarchical graphs, also leads to the emergence of multifractality, see, e.g. [64].

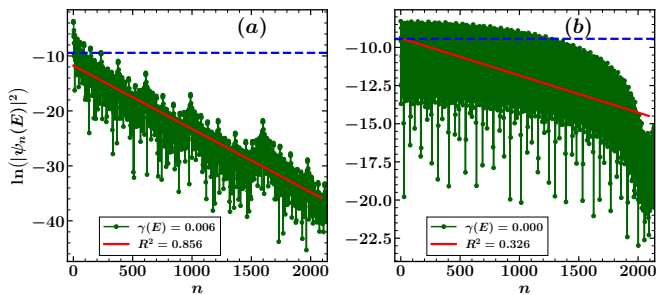


FIG. 4. Spatial decay profiles of two consecutive eigenstates. (a) A localized state with $E = -0.26$ exhibiting clear exponential decay, with $\gamma(E) = 0.006$ and a good linear fit ($R^2 = 0.856$). (b) The neighboring delocalized state with $E = -0.22$, characterized by $\gamma(E) \approx 0$ and poor linear fitting quality ($R^2 = 0.326$), indicating the absence of exponential localization. The dashed horizontal line marks the reference level $-\ln N$ of the ergodic wave function. Here averaging is done over 50 values of θ . Number of unit cells $L = 4181$, system size $N = 3L = 12543$, $\lambda = 10$, and $\epsilon_1 = 16.8$.

tions do not show exponential decay, resulting in significantly reduced values of R^2 . We therefore use the quality of the fit itself as a diagnostic to separate localized from delocalized states. We choose the critical value of $R_c^2 = 0.85$; the states with $R^2 \geq R_c^2$ are classified as exponentially localized and the states with $R^2 < R_c^2$ are identified as nonlocalized. For the latter, the extracted γ has no physical meaning since the exponential form is not applicable, hence we set γ to a negligibly small value (10^{-14}). To justify the chosen threshold R_c^2 , we examine the wavefunction profiles of two consecutive eigenstates across the localization transition. For the localized state [Fig. 4(a)] we obtain $R^2 = 0.856$, whereas for the subsequent delocalized state [Fig. 4(b)] the goodness-of-fit parameter drops sharply to 0.326. This procedure ensures that only states exhibiting genuine exponential localization contribute finite Lyapunov exponents.

Figures 3(d)–(f) show the θ -averaged Lyapunov exponent γ as a function of ϵ_1 and energy E for $\lambda = 10, 5$, and 2, respectively. These phase plots exhibit the same qualitative features observed in the fractal dimension maps. For $\lambda = 10$ and 5, in the regime $\epsilon_1 < \lambda$, we observe greenish regions between the analytically obtained MEs, where $\ln(\gamma)$ becomes slightly negative, indicating the presence of localized states. A similar behavior is observed for $\lambda = 2$, where localized states emerge between the green dashed lines. Although the Lyapunov exponent alone cannot distinguish between delocalized and multifractal states, since $\gamma(E) = 0$ in both cases, a combined analysis with the phase diagrams of the fractal dimension D_2 [Figs. 3(a)–(c)] confirms the presence of multifractal states in the regime $\epsilon_1 < \lambda$. To further confirm the presence of localized states as well as multifractal states between our predicted MEs in the $\epsilon_1 < \lambda$ regime, we further analyze their individual spatial decay profiles.

A. Spatial decay profiles

We begin by examining the regime $\epsilon_1 < \lambda$, where singularities appear in the transfer matrix of the effective one-dimensional model. To validate the observations from the phase diagrams, we plot the Lyapunov exponent $\gamma(E)$ for $\lambda = 10$ and $\epsilon_1 = 1.5$ [Fig. 5(a)]. The green dashed lines denote the AMEs predicted by Avila’s theory. Nonzero values of $\gamma(E)$ are observed between these AMEs, indicating localized behavior of the eigenstates and revealing a disagreement between the numerical and analytical results. In the $\epsilon_1 > \lambda$ regime, transfer matrix singularities are absent, and we observe conventional MEs separating localized and extended states [Fig. 5(b)]. Even in this regime, small but significantly non-zero $\gamma(E)$ values appear between the analytical MEs, demonstrating a quantitative deviation of Avila’s theory from the numerical results. To further confirm the nature of the eigenstates, we analyze the spatial decay of the wavefunction amplitudes by averaging $\langle \ln(|\psi_n(E)|^2) \rangle_E$ over eigenstates within specific energy intervals for various values of λ , where $\langle \cdot \rangle_E$ denotes averaging over eigenstates within the chosen energy interval.

For the localized states the wavefunction intensity decays exponentially as in Eq. (28). For multifractal states, the situation is more subtle. Although $\gamma(E)$ may approach zero in the thermodynamic limit, the wave function does not exhibit simple diffusive nature. Therefore, a power-law fit is more appropriate for characterizing such states. In this case, the probability density follows

$$|\psi_n(E)|^2 \sim \frac{1}{|n - n_0|^\mu}, \quad (29)$$

reflecting scale-invariant spatial fluctuations. The exponent μ is not directly related to the Lyapunov exponent but can serve as a useful indicator of the nature of the eigenstates. Specifically, the states are said to be power-law localized for $\mu > 1$, multifractal for $\mu \sim 1$, and ergodic for $\mu = 0$.

Figs. 5(c) and 5(d) represent this average for localized eigenstates with energies in the range $E \in [-0.3, -0.25]$ at $\epsilon_1 = 1.5$, and energies in the range $E \in [-0.28, -0.25]$ at $\epsilon_1 = 16.8$, shown by blue rectangles in the inset in panels (a) and (b), for $\lambda = 10$ with $\langle \gamma \rangle_E = 0.104$, and $\langle \gamma \rangle_E = 0.014$, respectively, exhibiting clear exponential decay. The corresponding positive LE, significantly larger than the inverse system size $1/N$, confirms the localized nature of these states. In contrast, Fig. 5(e) shows the same analysis for power-law-decaying eigenstates within the energy range $[-0.004, 0.004]$, for $\lambda = 10$ where the power-law decay exponent turns out to be $\mu = 0.789$ thus confirming the multifractal nature of these states. The existence of localized states, within the interval between the analytically predicted AMEs (MEs) in the $\epsilon_1 < \lambda$ ($\epsilon_1 > \lambda$) regime, signals the disagreement of Avila’s global theory approach of finding mobility edges, which assumes a strict separation of these phases. Furthermore, Fig. 5(f) does not show any decay indicating

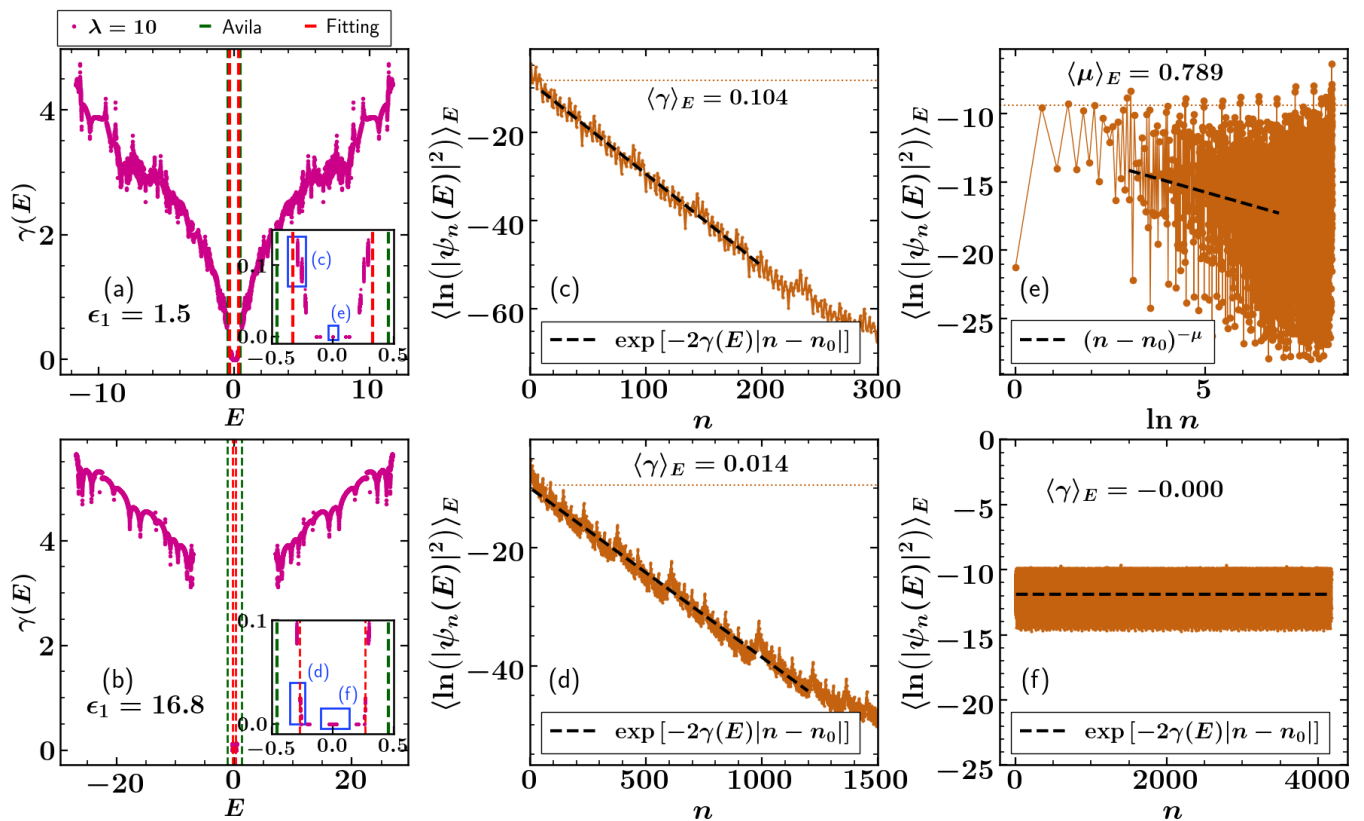


FIG. 5. (a), (b) Lyapunov exponent $\gamma(E)$ for all eigenstates with (a) $\epsilon_1 = 1.5$, and (b) $\epsilon_1 = 16.8$. The green dashed lines indicate analytically derived mobility edges using Avila's theory [Eq. (26)]. The red dashed lines are plotted using Eq. (31) obtained after the fitting procedure. (c)–(f) Averaged $\ln(|\psi_n(E)|^2)$ over eigenstates with energies within the specified intervals, plotted as a function of the distance n from the site of maximum amplitude ψ_{\max} . (c) For $\epsilon_1 = 1.5$, data averaged over $E \in [-0.3, -0.25]$; (d) for $\epsilon_1 = 16.8$, data averaged over $E \in [-0.28, -0.25]$, where the black dashed line denotes an exponential fit with $\langle \gamma \rangle_E = 0.104$ and $\langle \gamma \rangle_E = 0.014$, respectively showing exponential decay. (e) For $\epsilon_1 = 1.5$, data averaged over $E \in [-0.004, 0.004]$ where the black dashed line shows a power-law decay with exponents $\mu = 0.789$ indicating multifractal nature. (f) For $\epsilon_1 = 16.8$, data averaged over $E \in [-0.06, 0.06]$ with $\langle \gamma \rangle_E = 0$ showing delocalized behavior of states. The corresponding energy windows are highlighted by blue rectangles in panels (a) and (b). In all panels, averages are taken over 50 realizations of the phase parameter θ . The system parameters are fixed at $N = 12543$, $\lambda = 10$ and $J = 1$.

extended behavior of states in the $\epsilon_1 > \lambda$ regime which is consistent with our phase diagrams. Hence we can conclude the presence of AMEs in the $\epsilon_1 < \lambda$ regime and MEs in the $\epsilon_1 > \lambda$ regime. We further confirm these results by studying $\langle \gamma \rangle_E$ with system size in Appendix B using exact diagonalization. We have also confirmed these results by computing the LE directly using the transfer matrix, which yields consistent results.

VI. DISAGREEMENT WITH AVILA'S THEORY

In this section, we discuss in detail the disagreement between Avila's theoretical approach for determining mobility edges in one-dimensional systems and our numerical results. Our findings indicate that the analytical predictions of Avila's global theory agree only qualitatively but fail quantitatively. To achieve quantitative agreement, a fitting parameter must be introduced into the

expression derived from Avila's theory. The following subsection outlines the fitting protocol used for this purpose.

A. Quantitative disagreement: Fitting Protocol

To obtain an approximate analytical expression for the mobility edges by fitting form similar to Eq. (26), we analyze the phase plots of the Lyapunov exponent $\gamma(E)$, extracted from exponential fits to the spatial decay of individual eigenstates. As discussed above, only states exhibiting a robust exponential fit are assigned a finite Lyapunov exponent, while delocalized states are identified based on a low goodness of fit parameter R^2 . Using this classification, we determine the mobility edges as follows. For each value of ϵ_1 , we identify the highest absolute value of energy belonging to the delocalized regime and denote it by E_{\min} , and the lowest absolute value

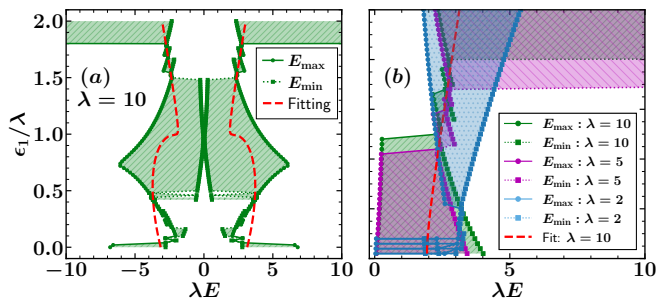


FIG. 6. (a) Offset ϵ_1 versus eigenenergy E showing the numerically obtained mobility edges E_{\min} and E_{\max} for $\lambda = 10$. (b) Comparison of E_{\min} and E_{\max} in $\epsilon_1 > \lambda$ regime for $\lambda = 10, 5$, and 2 , demonstrating the scaling form of the fitting expression in Eq. (31). Red dashed lines denote the fitting curves. The colored shaded region between E_{\min} and E_{\max} marks the allowed region for the mobility edge, with the shade color same as the corresponding λ curves. All quantities are averaged over 50 realizations of the phase parameter θ . The system size is $N = 12543$ and $J = 1$.

of energy belonging to the localized regime, denoted by E_{\max} . In Fig. 6(a) we plot both E_{\min} and E_{\max} as functions of ϵ_1 ; the points where these two curves meet define the approximate locations of the mobility edges. These extracted points are then fitted using a functional form inspired by Eq. (26). For $\lambda = 10$, in the $\epsilon_1 > \lambda$ regime we fit our data to the functional form

$$E = \frac{X\epsilon_1 + Y\sqrt{|\epsilon_1^2 - \lambda^2|}}{\lambda^2}. \quad (30)$$

The best-fit parameters are $X = 1.92 \pm 0.15$ and $Y = -0.46 \pm 0.15$ with goodness of fit parameter $R^2 = 0.98$. Since the mobility edge must remain continuous across the boundary at $\epsilon_1 = \lambda$, we impose the condition

$$\begin{aligned} E(\epsilon_1 = \lambda + 0) &= E(\epsilon_1 = \lambda - 0), \\ X_1 &= X_2. \end{aligned}$$

Accordingly, we fix $X_2 = X_1$ and fit only the coefficient Y_2 in the regime $\epsilon_1 < \lambda$, obtaining $Y_2 = 2.94 \pm 0.10$ with goodness of fit parameter $R^2 = 0.40$. The resulting fitted expression for the mobility edges is

$$|E| = \begin{cases} \frac{2\epsilon_1 + 3\sqrt{\lambda^2 - \epsilon_1^2}}{\lambda^2}, & \text{if } \epsilon_1 < \lambda, \\ \frac{2\epsilon_1 - 0.5\sqrt{\epsilon_1^2 - \lambda^2}}{\lambda^2}, & \text{if } \epsilon_1 > \lambda. \end{cases} \quad (31)$$

To test the validity of this fitted form, we compare it with the numerically obtained E_{\max} and E_{\min} for $\lambda = 10, 5$, and 2 , in the $\epsilon_1 > \lambda$ regime only, in the same plot in Fig. 6(b). We have shown data and fitting only for $E > 0$, as energies are symmetric around $E = 0$. The shaded region between E_{\min} and E_{\max} marks the allowed region for the mobility edge (red fitted line). For $\lambda = 10$, and 5 the fitted curve clearly separates E_{\max} from E_{\min} , indicating good agreement with numerical results. In contrast,

for $\lambda = 2$, the fitted expression fails to provide such a separation signaling a breakdown of the fitting in this regime. The same behavior is also evident in the phase diagrams shown in Fig. 3. In particular, for larger values of λ ($\lambda = 10$ and 5), the fitted mobility edges (red dashed lines) reproduce the numerical phase boundaries reasonably well in the $\epsilon_1 > \lambda$ regime. However, in the $\epsilon_1 < \lambda$ regime, the fit fails to completely separate localized states from multifractal ones [red dashed lines in Fig. 5(a)], since the functional form used for fitting is derived specifically for the $\epsilon_1 > \lambda$ region. Moreover, for smaller values of λ (e.g., $\lambda = 2$), the fitted expression no longer reproduces the observed ME structure and becomes unreliable. This indicates a qualitative breakdown of Avila's theoretical framework for $\lambda \lesssim 2$. We further examine this deviation through the spatial decay analysis for $\lambda = 2$ in the next subsection.

B. Qualitative Disagreement: $\lambda = 2$

Here, we examine the qualitative breakdown of Avila's theoretical framework for $\lambda \lesssim 2$. From the phase plots for $\lambda = 2$, we observe that both the expressions obtained from Avila's theory (green dotted lines) and those obtained after fitting (red dashed lines) fail to separate localized and extended states in the $\epsilon_1 > \lambda$ regime [Figs. 3(c) and (f)]. In contrast, in the $\epsilon_1 < \lambda$ regime, not only do these analytical expressions fail to remain exact, but also failed to predict the presence of multiple mobility edges. To confirm these observations, we analyze the spatial decay of eigenstates for various energy ranges for $\lambda = 2$. Figure 7(a) corresponds to $\epsilon_1 = 1$, which lies in the $\epsilon_1 < \lambda$ regime. We observe the presence of AMEs separating localized and multifractal states. Across the energy spectrum, the Lyapunov exponent γ exhibits multiple points where it vanishes and reappears, indicating the presence of several AMEs. The AME between localized and multifractal states is further confirmed by examining the spatial decay of wave functions at different energies [Figs. 7(c) and 7(e)]. In contrast, for $\epsilon_1 = 2.2$ (in the $\epsilon_1 > \lambda$ regime), both localized and delocalized states are separated by the conventional ME [Figs. 7(d) and 7(f)]. As shown in Fig. 7(b), both the analytical and fitted expressions fail to separate these states. Collectively, these results demonstrate that for $\lambda \lesssim 2$, Avila's theory breaks down even qualitatively.² This disagreement with Avila's theory is further supported by the IPR collapse analysis presented in Appendix D. Results for a single realization of θ are presented in Appendix E, confirming that our conclusions do not depend on phase averaging.

² Note that already at $\lambda = 10$ the multiple AMEs start to emerge, see, e.g., the results at $\epsilon_1 = 4.4$ in Appendix C.

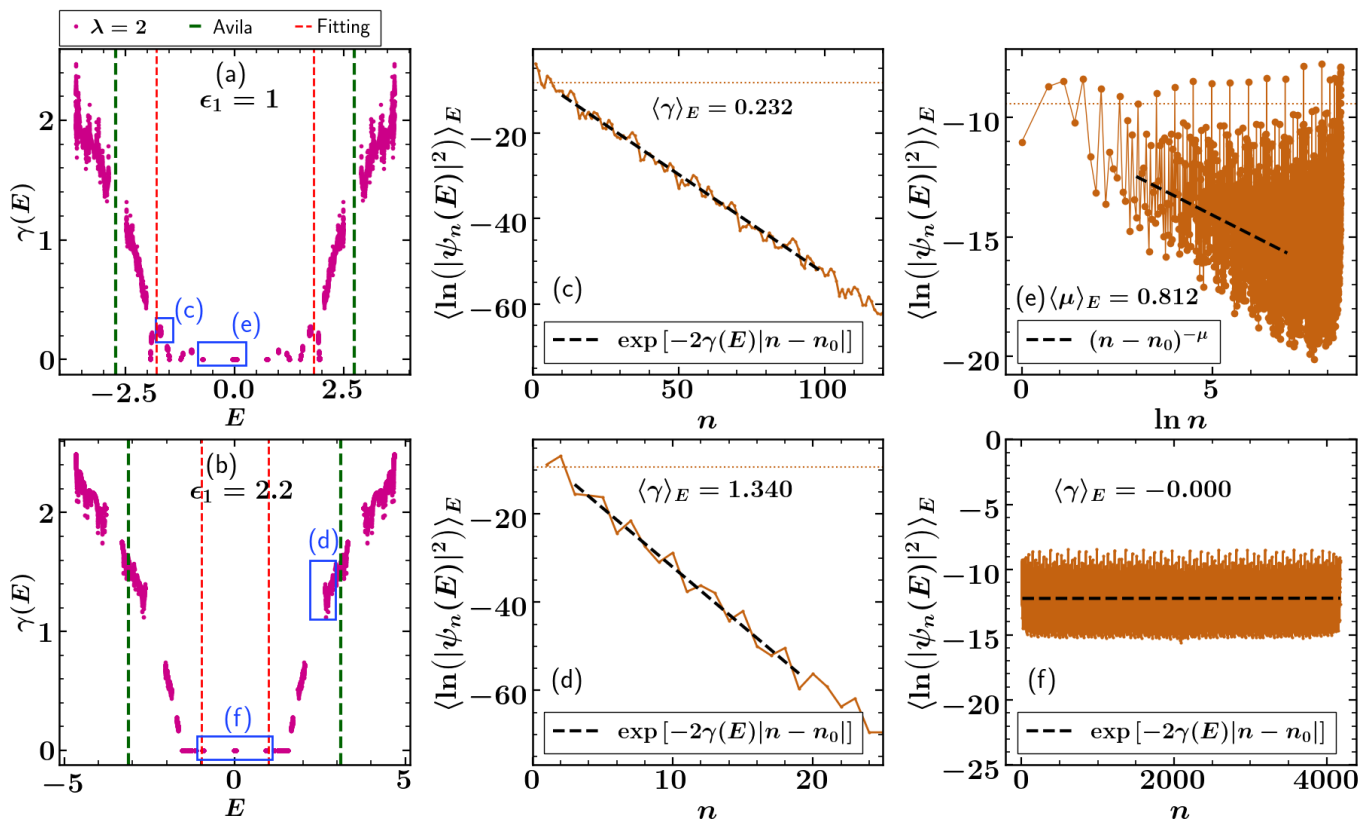


FIG. 7. (a), (b) Lyapunov exponent $\gamma(E)$ for all eigenstates with (a) $\epsilon_1 = 1$, and (b) $\epsilon_1 = 2.2$. The green dashed lines indicate analytically derived mobility edges using Avila's theory [Eq. (26)]. The red dashed lines are plotted using Eq. (31) obtained after the fitting procedure. (c)–(f) Averaged $\ln(|\psi_n(E)|^2)$ over eigenstates with energies within the specified intervals, plotted as a function of the distance n from the site of maximum amplitude ψ_{\max} . (c) For $\epsilon_1 = 1$, data averaged over $E \in [-1.8, -1.6]$; (d) for $\epsilon_1 = 2.2$, data averaged over $E \in [2.5, 3.0]$, where the black dashed line denotes an exponential fit with $\langle\gamma\rangle_E = 0.232$ and $\langle\gamma\rangle_E = 1.340$, respectively showing exponential decay. (e) For $\epsilon_1 = 1$, data averaged over $E \in [-0.75, 0.25]$ where the black dashed line shows a power-law decay with exponents $\mu = 0.821$ indicating multifractal nature. (f) For $\epsilon_1 = 2.2$, data averaged over $E \in [-1.0, 1.0]$ with $\langle\gamma\rangle_E = 0$ showing delocalized behavior of states. The corresponding energy windows are highlighted by blue rectangles in panels (a) and (b). In all panels, averages are taken over 50 realizations of the phase parameter θ . The system parameters are fixed at $N = 12543$, $\lambda = 2$ and $J = 1$.

VII. CONCLUSION

We investigate the emergence and nature of mobility edges in the ABF diamond chain subjected to a quasiperiodic Aubry-André potential with an additional constant offset, where the potential is applied antisymmetrically to top and bottom sites. Our study reveals two distinct types of mobility edges: (i) anomalous mobility edges separating localized and multifractal states in the regime $\epsilon_1 < \lambda$, and (ii) conventional MEs separating localized and ergodic (delocalized) states in the regime $\epsilon_1 > \lambda$. These results are obtained through fractal dimension analysis and are further supported by numerical calculations of the Lyapunov exponent using both exact diagonalization and the transfer matrix method. To further characterize the multifractal states, we analyze the power law decay of the wave function amplitude and extract the associated decay exponent.

Additionally, we derive an analytical expression for the

MEs based on Avila's global theory. While the expression reproduces previous results for systems without an offset, the theory agrees only qualitatively for $\lambda \gtrsim 2$ and fails quantitatively when an offset is introduced. To achieve quantitative agreement, we incorporate fitting parameters into the analytical formula, which successfully captures the numerical results for $\lambda > 2$ in $\epsilon_1 > \lambda$ regime. However, even after fitting, the analytical formula fails quantitatively in the regime $\epsilon_1 < \lambda$. For $\lambda \lesssim 2$, Avila's theory fails even qualitatively due to the presence of multiple mobility edges in the $\epsilon_1 < \lambda$ regime. The breakdown of Avila's theory in the regime $\epsilon_1 < \lambda$ may be attributed to the massive degeneracy in the all-bands-flat diamond chain. Although the antisymmetric on-site potential lifts the exact degeneracy, for small ϵ_1 and small λ the resulting energy levels remain strongly clustered, reflecting their flat-band origin. Our work provides the first demonstration of this limitation in the application of Avila's formalism for determining mobility edges in

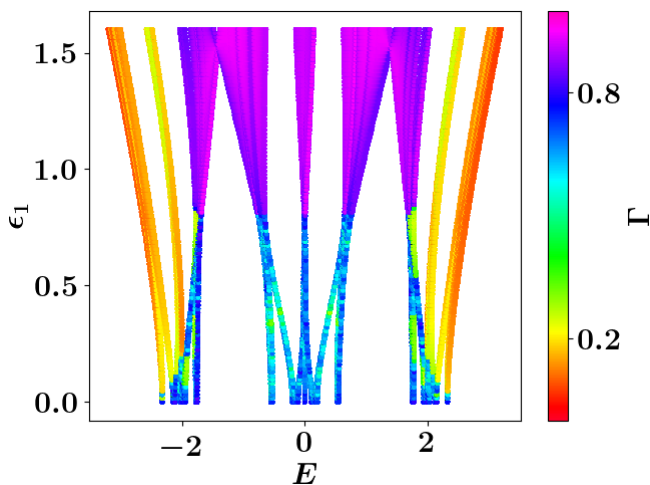


FIG. 8. ϵ_1 - E phase diagram for $\lambda = 0.8$, where the color scale represents the fractal dimension. Data is averaged over 50 realizations of the phase parameter θ , with $N = 12543$ and $J = 1$. The analytical predictions using Eq. (26) are not visible as they lie far outside the spectral boundaries.

flat-band systems with an offset potential.

ACKNOWLEDGMENTS

We are grateful to the High Performance Computing (HPC) facility at IISER Bhopal, where most of calculations in this project were run. M.K is grateful to the Council of Scientific and Industrial Research (CSIR), India, for his PhD fellowship.

Appendix A: Phase plot for $\lambda = 0.8$

To further illustrate the qualitative disagreement between Avila's theory and numerical results for small values of λ , we plot the ϵ_1 - E phase diagram with the fractal dimension D_2 for $\lambda = 0.8$, as shown in Fig. 8. We observe both multifractal and localized states in the $\epsilon_1 < \lambda$ regime, and extended as well as localized states in the $\epsilon_1 > \lambda$ regime. In contrast, the analytical predictions from Avila's theory are not visible in the phase plot, as the corresponding mobility edge lines lie outside the spectral boundaries, implying that all states are multifractal for $\epsilon_1 < \lambda$. A similar behavior is observed for $\epsilon_1 = 0$; for $\lambda \lesssim 1.5$, all states become multifractal. These results highlight a significant qualitative breakdown of Avila's analytical expression when compared with the numerical findings.

Appendix B: Lyapunov exponent with system size

In this section, we study the Lyapunov exponent using exact diagonalization by examining the exponential de-

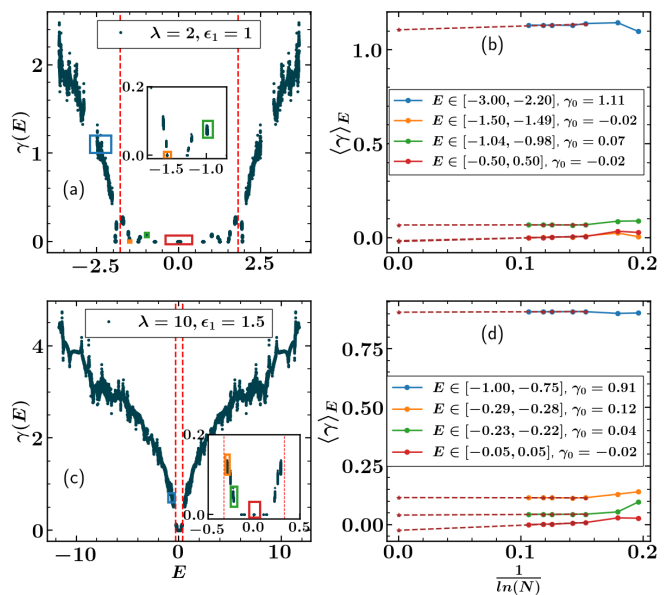


FIG. 9. Average Lyapunov exponent analysis with system size for $\epsilon_1 < \lambda$ regime. For $\lambda = 2$, (a) $\gamma(E)$ for all eigenstates with $\epsilon_1 = 1$ and (b) average $\langle \gamma \rangle_E$ with $1/\ln N$ in different energy ranges. Panels (c,d) show the same quantities for $\lambda = 10$ with $\epsilon_1 = 1.5$. In panel (a) and (c), red dashed lines are analytical results using Eq. (31). Different energy windows used in panels (b) and (d) are indicated in panels (a) and (c), respectively, by rectangular boxes with same colors. In all panels, averages are taken over 50 realizations of the phase parameter θ , with $N = 12543$, and $J = 1$.

ca of the wavefunction amplitudes [Eq. (28)], and focus on the Lyapunov exponent as a function of system size, to further confirm the nature of the eigenstates. To this end, we compute the energy averaged Lyapunov exponent $\langle \gamma \rangle_E$ over different energy intervals corresponding to distinct spectral regions. We then evaluate $\langle \gamma \rangle_E$ for various system sizes and plot it as a function of $1/\ln(N)$. The extrapolation of this curve to $1/\ln(N) \rightarrow 0$ yields the thermodynamic-limit value $\gamma_{N \rightarrow \infty}$. For localized states, $\gamma_{N \rightarrow \infty} > 0$, whereas for extended and multifractal states, $\gamma_{N \rightarrow \infty} \leq 0$. In addition to the exact diagonalization results, we also computed the Lyapunov exponent directly using the transfer matrix method. The results of this analysis qualitatively agree with those obtained from exact diagonalization, further supporting the robustness of our numerical results.

1. $\epsilon_1 < \lambda$

We first examine the $\epsilon_1 < \lambda$ regime, where anomalous mobility edges (AMEs) are observed separating localized and delocalized states. Figures 9(a)-(b) show results for $\lambda = 2$ and $\epsilon_1 = 1$. The Lyapunov exponents are averaged over successive energy intervals from left to right across the spectrum shown by coloured boxes. A key observation is that $\gamma_0 \equiv \gamma_{N \rightarrow \infty} = -0.02$

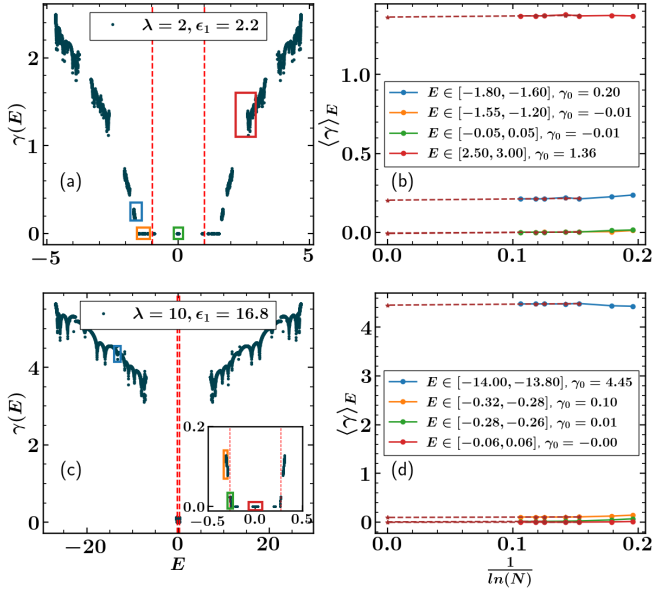


FIG. 10. Average Lyapunov exponent analysis with system size for $\epsilon_1 > \lambda$ regime. For $\lambda = 2$, (a) $\gamma(E)$ for all eigenstates with $\epsilon_1 = 2.2$ and (b) average $\langle \gamma \rangle_E$ with $1/\ln N$ in different energy ranges. Panels (c,d) show the same quantities for $\lambda = 10$ with $\epsilon_1 = 16.8$. In panel (a) and (c), red dashed lines are analytical results using Eq. (31). Different energy windows used in panels (b) and (d) are indicated in panels (a) and (c), respectively, by rectangular boxes with same colors. In all panels, averages are taken over 50 realizations of the phase parameter θ , with $N = 12543$, and $J = 1$.

(≈ 0) for $E \in [-1.50, -1.49]$, indicating multifractal behavior in this range. Subsequently, $\gamma_0 = 0.07$ for $E \in [-1.04, -0.98]$, signifying localization, and again $\gamma_0 \approx 0$ for $E \in [-0.05, 0.05]$, corresponding to multifractal states. These results clearly demonstrate the presence of multiple AMEs for $\lambda = 2$, a feature not captured by Avila's theory. For comparison, Figs. 9(c)-(d) show the results for $\lambda = 10$ and $\epsilon_1 = 1.5$, which again confirm the presence of AMEs in the $\epsilon_1 < \lambda$ regime, consistent with our observations in the main text.

2. $\epsilon_1 > \lambda$

Here, we present a similar analysis in the $\epsilon_1 > \lambda$ regime to confirm the presence of MEs separating localized and extended states. Figures 10(a)-(b) show the results for $\lambda = 2$ and $\epsilon_1 = 2.2$, where both $\gamma_0 \equiv \gamma_{N \rightarrow \infty} > 0$ and $\gamma_0 \approx 0$ are observed, indicating the coexistence of localized and extended states. It is also noteworthy that the analytically predicted MEs (red dashed lines in Fig. 10(a)) fail to separate localized and extended states, demonstrating the breakdown of the analytical results for $\lambda \lesssim 2$. Furthermore, the presence of MEs is also evident for $\lambda = 10$ and $\epsilon_1 = 16.8$, as shown in Figs. 10(c)-(d). These results are consistent with the phase diagrams presented in the main text.

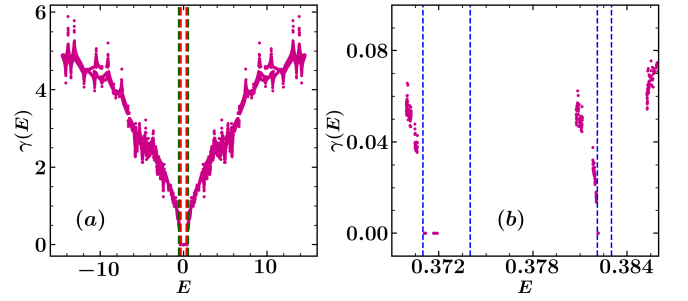


FIG. 11. (a) Lyapunov exponent $\gamma(E)$ for all eigenstates with $\epsilon_1 = 4.4$ and $\lambda = 10$. Green dashed lines denote analytically obtained mobility edges, and red dashed lines correspond to the fitted mobility edges from Eq. (31). (b) Zoomed view of panel (a) highlighting multiple AMEs. The blue dashed lines are guides for eyes drawn to separate multifractal states from delocalized states. In all panels, data are averaged over 50 realizations of the phase parameter θ , with $N = 12543$ and $J = 1$.

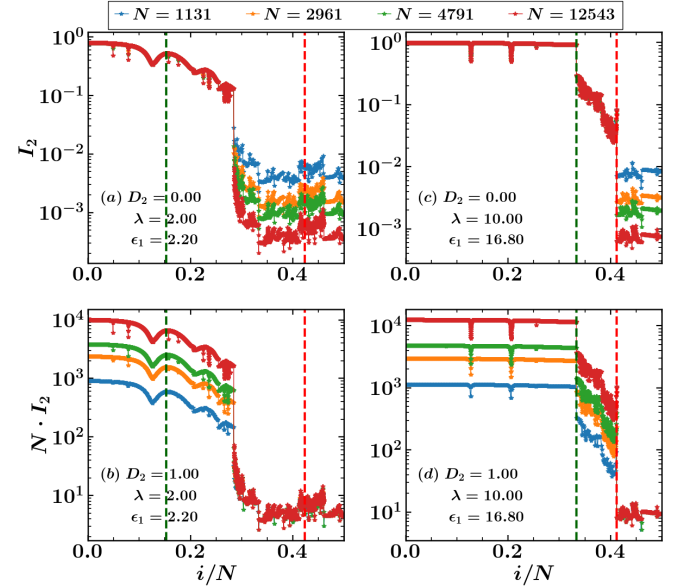


FIG. 12. IPR collapse plots for different system sizes in $\epsilon_1 > \lambda$ regime. The horizontal axis represents the normalized eigenstate index i/N . The vertical axis represents $(N^{D_2} I_2)$ for (a)-(b) $\lambda = 2$, $\epsilon_1 = 2.2$, and (c)-(d) $\lambda = 10$, $\epsilon_1 = 16.8$ with $D_2 = 1$ for (a, c) and $D_2 = 0$ for (b, d). The green dashed lines indicate analytically derived mobility edges using Avila's theory [Eq. (26)]. The red dashed lines are plotted using Eq. (31) obtained after the fitting procedure. In all panels, averages are taken over 50 realizations of the phase parameter θ . $J = 1$.

Appendix C: Multiple Mobility edges for $\lambda = 10$: $\epsilon_1 = 4.4$ case

In this appendix, we present a representative case with $\lambda = 10$ and $\epsilon_1 = 4.4$, where multiple anomalous mobility edges are observed. Figure 11(a) shows the Lyapunov exponent $\gamma(E)$ calculated for all eigenstates at these parameter values. As expected, multifractal states appear

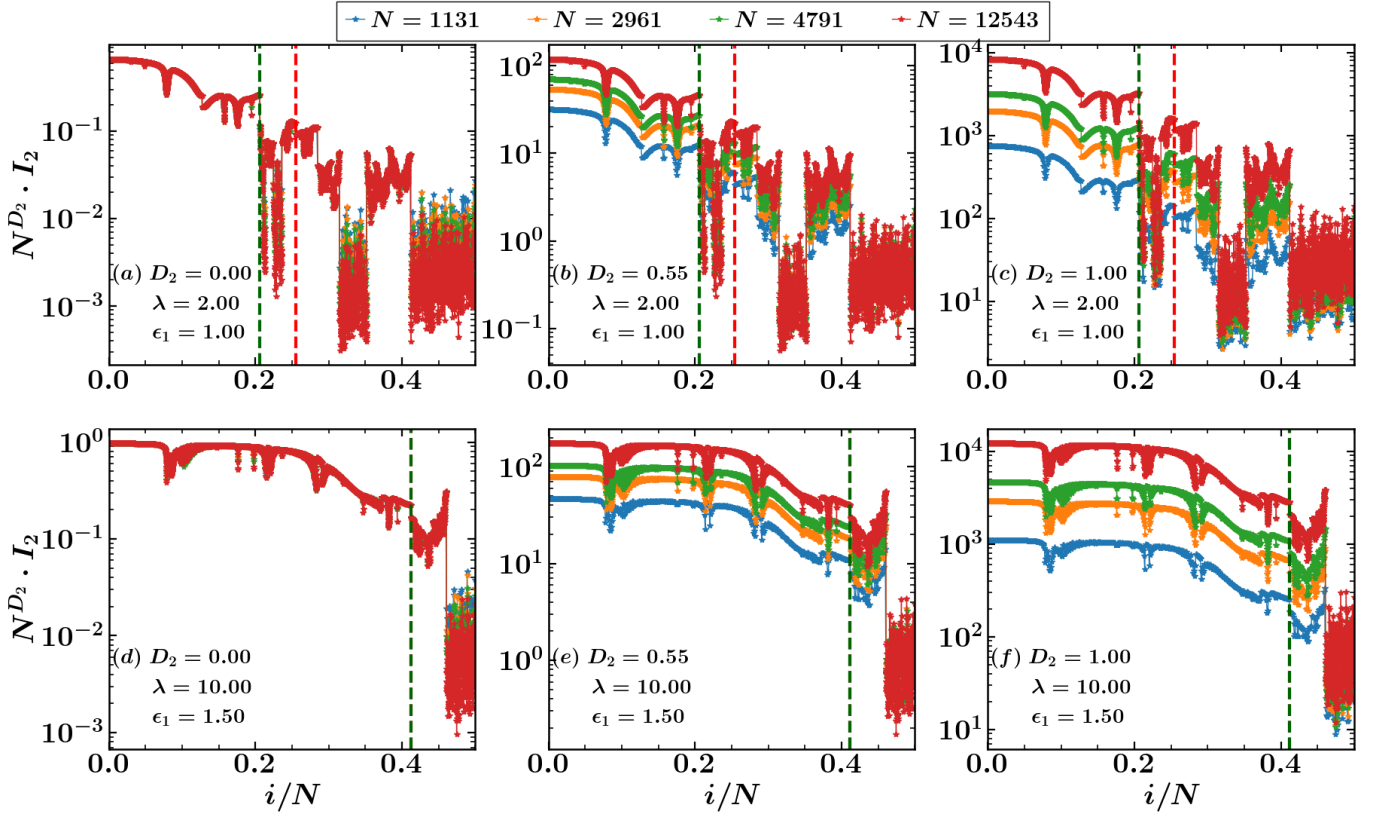


FIG. 13. IPR collapse plots for different system sizes in $\epsilon_1 < \lambda$ the regime. The horizontal axis represents the normalized eigenstate index i/N . The vertical axis represents $(N^{D_2} I_2)$ for (a)-(b) $\lambda = 2$, $\epsilon_1 = 1.0$, and (c)-(d) $\lambda = 10$, $\epsilon_1 = 1.50$, with $D_2 = 0$ for (a, d), $D_2 = 0.55$ for (b, e), and $D_2 = 1$ for (c, f). The green dashed lines indicate analytically derived mobility edges using Avila's theory [Eq. (26)]. The red dashed lines are plotted using Eq. (31) obtained after the fitting procedure. In all panels, averages are taken over 50 realizations of the phase parameter θ and $J = 1$.

within the red dashed AMEs obtained from Eq. (31). In addition to these predicted edges, we identify further multifractal regions in the narrow energy intervals $0.371 < E < 0.373$ and $0.382 < E < 0.383$, as shown in Fig. 11(b). These intervals are marked by blue dashed lines. Outside these windows, the Lyapunov exponent becomes finite, indicating localized states. Notably, these additional multifractal regions lie outside the red dashed AMEs predicted by the analytical expression. A symmetric set of anomalous mobility edges is also observed at negative energies, specifically within $-0.373 < E < -0.371$ and $-0.383 < E < -0.382$. These results demonstrate that, already at $\lambda = 10$, the system exhibits multiple anomalous mobility edges, indicating a qualitative deviation from the predictions of Avila's theory.

Appendix D: IPR collapse analysis

In this section we study scaling of inverse participation ratio with system size to explore the behavior of eigenstates. For a system of size N , the IPR scales as $I_2 \sim N^{-D_2}$, where D_2 is the fractal dimension. Local-

ized states exhibit $D_2 = 0$, yielding an IPR independent of system size, whereas fully extended (delocalized) states have $D_2 = 1$, for which $I_2 \propto 1/N$. Accordingly, plotting $(N^{D_2} I_2)$ for different system sizes results in a data collapse when the correct D_2 is chosen: the curves collapse at $D_2 = 0$ for localized states and at $D_2 = 1$ for delocalized states. For multifractal states to collapse, one can calculate D_2 using

$$D_2 = -\frac{\ln \langle I_2 \rangle_E}{\ln N}. \quad (\text{D1})$$

We perform this IPR scaling analysis for multiple system sizes to identify the presence of mobility edges.

1. $\epsilon_1 > \lambda$

We first examine the regime $\epsilon_1 > \lambda$, where conventional MEs separate localized and delocalized states. Figures 12(a)-(b) correspond to $\lambda = 2$ and $\epsilon_1 = 2.2$ for $D_2 = 0$ and $D_2 = 1$, respectively. The data collapse of different system sizes in Fig. 12(a) confirms the localized nature of the states ($D_2 = 0$), whereas the collapse in Fig. 12(b) indicates extended states ($D_2 = 1$). Only half

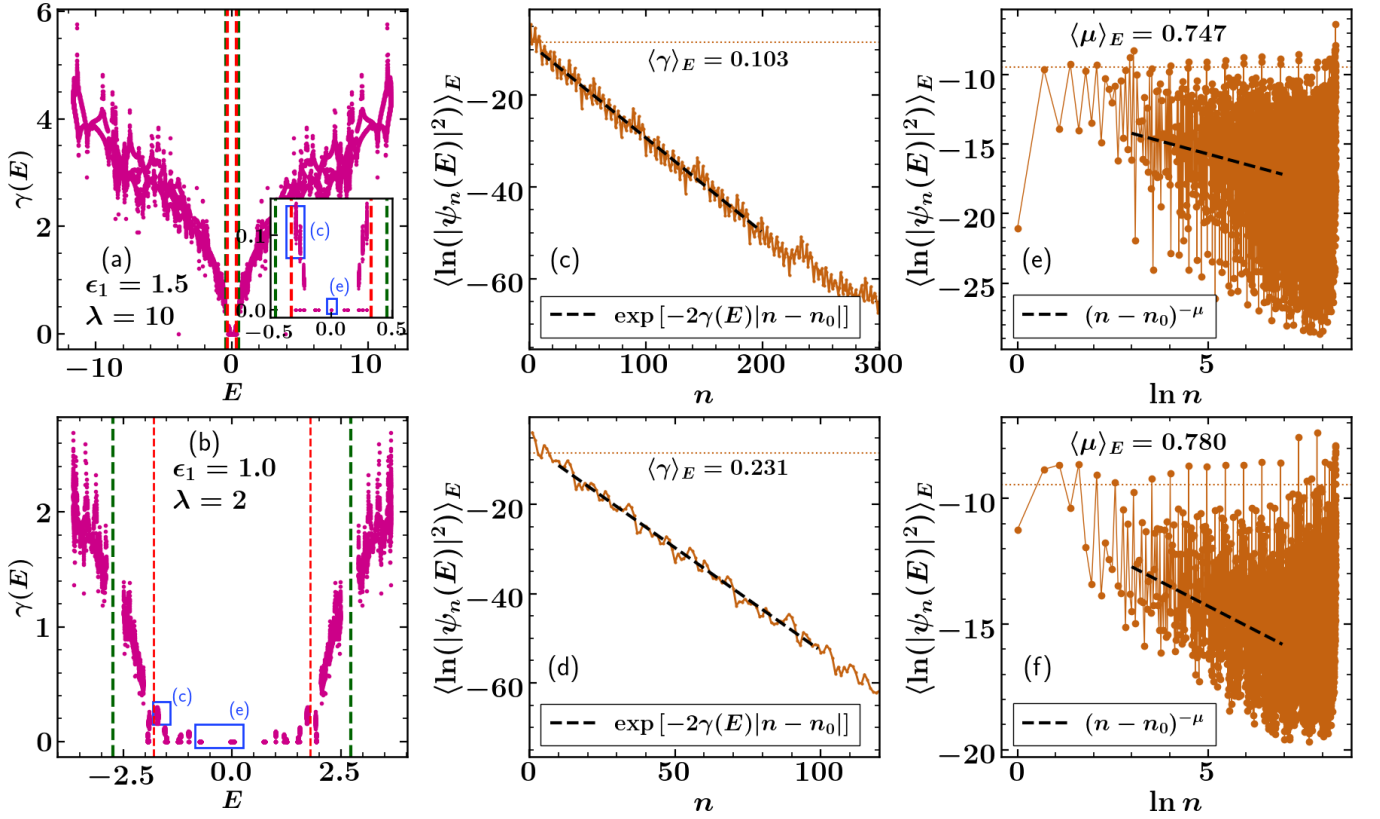


FIG. 14. (a),(b) Lyapunov exponent $\gamma(E)$ for all eigenstates with (a) $\lambda = 10$, $\epsilon_1 = 1.5$ and (b) $\lambda = 2$, $\epsilon_1 = 1.0$. The green dashed lines indicate analytically derived mobility edges using Avila's theory [Eq. (26)]. The red dashed lines are plotted using Eq. (31) obtained after the fitting procedure. (c)–(f) Averaged $\ln(|\psi_n(E)|^2)$ over eigenstates with energies in the specified intervals, plotted as a function of the distance n from the site of maximum amplitude ψ_{\max} . Panels (c) and (d) correspond to the energy windows $E \in [-0.3, -0.25]$ for $\lambda = 10$, $\epsilon_1 = 1.5$ and $E \in [-1.8, -1.6]$ for $\lambda = 2$, $\epsilon_1 = 1.0$, respectively. In both cases, the black dashed line represents an exponential fit, yielding $\langle \gamma \rangle_E = 0.101$ and $\langle \gamma \rangle_E = 0.231$, demonstrating exponential decay. Panels (e) and (f) correspond to $E \in [-0.004, 0.004]$ for $\lambda = 10$, $\epsilon_1 = 1.5$ and $E \in [-0.75, 0.25]$ for $\lambda = 2$, $\epsilon_1 = 1.0$, respectively. Here the black dashed line indicates a power-law decay with exponents $\langle \mu \rangle_E = 0.944$ and $\langle \mu \rangle_E = 0.780$, indicating the multifractal nature of the states. In all panels, results are shown for a single random realization of θ which is taken to be 3.5714. Other parameters are $N = 12543$ and $J = 1$.

of the spectrum is shown, as the other half is symmetric. Similarly, Figs. 12(c)-(d) show results for $\lambda = 10$ and $\epsilon_1 = 16.8$, where the same behavior is observed: localized states collapse for $D_2 = 0$ and delocalized states collapse for $D_2 = 1$. Hence, in this regime, only localized and extended states exist. Notably, the expression obtained from Avila's theory (green dashed lines) fails to quantitatively separate localized and delocalized states, showing only qualitative agreement. In contrast, the fitted expression (red dashed lines) accurately captures the mobility edge for large $\lambda = 10$, but deviates for smaller $\lambda = 2$, consistent with the results presented in the main text.

2. $\epsilon_1 < \lambda$

Next, we focus on the $\epsilon_1 < \lambda$ regime and present the numerical results of the collapse analysis. Figures 13(a)-

(c) correspond to $\lambda = 2$ and $\epsilon_1 = 1$. The data collapse for different system sizes in Fig. 13(a) confirms the localized nature of the states. In contrast, Fig. 13(c), plotted for $D_2 = 1$, shows no collapse, indicating the absence of extended states in this regime. To determine D_2 for multifractal states, we plot $\ln\langle I_2 \rangle_E$ versus $\ln(N)$ and extract the slope from a linear fit, yielding a fractal dimension $D_2 = 0.54 \pm 0.027$. Using this value in Fig. 13(b), the data collapse confirms the presence of multifractal states. Moreover, multiple regions in the energy spectrum exhibit multifractal behavior, confirming the existence of multiple mobility edges in the $\epsilon_1 < \lambda$ regime for $\lambda = 2$. Figures 13(d)-(f) show similar behavior, further establishing the presence of AMEs separating localized and multifractal states. Importantly, for $\lambda = 2$, the presence of multiple AMEs indicates that Avila's theory fails even qualitatively, consistent with our findings in the main text.

Appendix E: Results for single θ realization

In the main text, all the numerical results are averaged over 50 realizations of the phase parameter θ . To demonstrate that our conclusions do not depend on phase averaging, we present results obtained from a single random realization of θ . For this purpose, we chose a random value $\theta = 3.5714$ within the interval $[0, 2\pi]$. Fig. 14 shows the Lyapunov exponent data for $\lambda = 10$ and $\lambda = 2$ in the regime $\epsilon_1 < \lambda$, corresponding to $\epsilon_1 = 1.4$ and $\epsilon_1 = 1.0$, respectively. For the single realization, the structure of the energy spectrum remains almost unchanged. In particular, the positions of the multiple anomalous mobility edges observed for $\lambda = 2$ [Fig. 14(b)] coincide closely with those obtained from the averaged data [Fig. 7(a)]. While minor fluctuations in individual multifractal states are visible, they do not affect the location of the mobility edges.

We further compute the energy averaged Lyapunov exponent $\langle \gamma \rangle_E$ by performing exponential fits over eigenstates within the same energy intervals used in the phase averaged analysis. Figures 14(c) and 14(e) show, respectively, exponential decay with $\langle \gamma \rangle_E = 0.103$ and power-law decay with $\langle \mu \rangle_E = 0.747$. This may be compared with the values $\langle \gamma \rangle_E = 0.104$, $\langle \mu \rangle_E = 0.789$, respectively, for $\lambda = 10$ and $\epsilon_1 = 1.5$ as obtained in the figures 5(c) and 5(e) where an averaging over 50 realizations of θ has been carried out. A similarly good agreement is observed for $\lambda = 2$ and $\epsilon_1 = 1.0$, as shown in Figs. 14(d)–14(f), which are also close to the corresponding θ -averaged results [see Fig. 7(c) and 7(e)]. We have verified that this consistency persists across other parameter sets as well. These results confirm that the mobility edge structure and the associated phase characterization are robust and are not an artifact of the θ -averaging over the phase parameter θ .

-
- [1] P. W. Anderson, Absence of diffusion in certain random lattices, *Phys. Rev.* **109**, 1492 (1958).
- [2] S. Aubry and G. André, Analyticity breaking and anderson localization in incommensurate lattices, *Ann. Isr. Phys. Soc.* **3**, 133 (1980).
- [3] S. Das Sarma, S. He, and X. C. Xie, Mobility edge in a model one-dimensional potential, *Phys. Rev. Lett.* **61**, 2144 (1988).
- [4] Y. Hashimoto, K. Niizeki, and Y. Okabe, A finite-size scaling analysis of the localization properties of one-dimensional quasiperiodic systems, *Journal of Physics A: Mathematical and General* **25**, 5211 (1992).
- [5] D. J. Boers, B. Goedeke, D. Hinrichs, and M. Holthaus, Mobility edges in bichromatic optical lattices, *Phys. Rev. A* **75**, 063404 (2007).
- [6] J. Biddle, B. Wang, D. J. Priour, and S. Das Sarma, Localization in one-dimensional incommensurate lattices beyond the aubry-andré model, *Phys. Rev. A* **80**, 021603 (2009).
- [7] J. Biddle and S. Das Sarma, Predicted mobility edges in one-dimensional incommensurate optical lattices: An exactly solvable model of anderson localization, *Phys. Rev. Lett.* **104**, 070601 (2010).
- [8] S. Lellouch and L. Sanchez-Palencia, Localization transition in weakly interacting bose superfluids in one-dimensional quasiperiodic lattices, *Phys. Rev. A* **90**, 061602 (2014).
- [9] X. Li, X. Li, and S. Das Sarma, Mobility edges in one-dimensional bichromatic incommensurate potentials, *Phys. Rev. B* **96**, 085119 (2017).
- [10] H. Yao, A. Khoukli, L. Bresque, and L. Sanchez-Palencia, Critical behavior and fractality in shallow one-dimensional quasiperiodic potentials, *Phys. Rev. Lett.* **123**, 070405 (2019).
- [11] S. Ganeshan, J. H. Pixley, and S. Das Sarma, Nearest neighbor tight binding models with an exact mobility edge in one dimension, *Phys. Rev. Lett.* **114**, 146601 (2015).
- [12] Z. Xu, H. Huangfu, Y. Zhang, and S. Chen, Dynamical observation of mobility edges in one-dimensional incommensurate optical lattices, *New Journal of Physics* **22**, 013036 (2020).
- [13] Y. Liu, X.-P. Jiang, J. Cao, and S. Chen, Non-hermitian mobility edges in one-dimensional quasicrystals with parity-time symmetry, *Phys. Rev. B* **101**, 174205 (2020).
- [14] Q.-B. Zeng and Y. Xu, Winding numbers and generalized mobility edges in non-hermitian systems, *Phys. Rev. Res.* **2**, 033052 (2020).
- [15] X. Deng, S. Ray, S. Sinha, G. V. Shlyapnikov, and L. Santos, One-dimensional quasicrystals with power-law hopping, *Phys. Rev. Lett.* **123**, 025301 (2019).
- [16] M. Saha, S. K. Maiti, and A. Purkayastha, Anomalous transport through algebraically localized states in one dimension, *Phys. Rev. B* **100**, 174201 (2019).
- [17] N. Roy and A. Sharma, Fraction of delocalized eigenstates in the long-range aubry-andré-harper model, *Phys. Rev. B* **103**, 075124 (2021).
- [18] H. Yin, J. Hu, A.-C. Ji, G. Juzeliūnas, X.-J. Liu, and Q. Sun, Localization driven superradiant instability, *Phys. Rev. Lett.* **124**, 113601 (2020).
- [19] Y. Wang, X. Xia, L. Zhang, H. Yao, S. Chen, J. You, Q. Zhou, and X.-J. Liu, One-dimensional quasiperiodic mosaic lattice with exact mobility edges, *Phys. Rev. Lett.* **125**, 196604 (2020).
- [20] X.-C. Zhou, Y. Wang, T.-F. J. Poon, Q. Zhou, and X.-J. Liu, Exact new mobility edges between critical and localized states, *Phys. Rev. Lett.* **131**, 176401 (2023).
- [21] L. Zhou, H. Pu, and W. Zhang, Anderson localization of cold atomic gases with effective spin-orbit interaction in a quasiperiodic optical lattice, *Phys. Rev. A* **87**, 023625 (2013).
- [22] M. Kohmoto and D. Tobe, Localization problem in a quasiperiodic system with spin-orbit interaction, *Phys. Rev. B* **77**, 134204 (2008).
- [23] R. S. Whitney, Most efficient quantum thermoelectric at finite power output, *Phys. Rev. Lett.* **112**, 130601 (2014).
- [24] K. Yamamoto, A. Aharony, O. Entin-Wohlman, and N. Hatano, Thermoelectricity near anderson localization

- transitions, *Phys. Rev. B* **96**, 155201 (2017).
- [25] C. Chiaracane, M. T. Mitchison, A. Purkayastha, G. Haack, and J. Goold, Quasiperiodic quantum heat engines with a mobility edge, *Phys. Rev. Res.* **2**, 013093 (2020).
- [26] Y. Lahini, R. Pugatch, F. Pozzi, M. Sorel, R. Morandotti, N. Davidson, and Y. Silberberg, Observation of a localization transition in quasiperiodic photonic lattices, *Phys. Rev. Lett.* **103**, 013901 (2009).
- [27] J. E. Lye, L. Fallani, M. Modugno, D. S. Wiersma, C. Fort, and M. Inguscio, Bose-einstein condensate in a random potential, *Phys. Rev. Lett.* **95**, 070401 (2005).
- [28] E. Lucioni, B. Deissler, L. Tanzi, G. Roati, M. Zaccanti, M. Modugno, M. Larcher, F. Dalfovo, M. Inguscio, and G. Modugno, Observation of subdiffusion in a disordered interacting system, *Phys. Rev. Lett.* **106**, 230403 (2011).
- [29] M. Schreiber, S. S. Hodgman, P. Bordia, H. P. Lüschen, M. H. Fischer, R. Vosk, E. Altman, U. Schneider, and I. Bloch, Observation of many-body localization of interacting fermions in a quasirandom optical lattice, *Science* **349**, 842 (2015).
- [30] V. Oganesyan and D. A. Huse, Localization of interacting fermions at high temperature, *Phys. Rev. B* **75**, 155111 (2007).
- [31] F. Alet and N. Laflorencie, Many-body localization: An introduction and selected topics, *Comptes Rendus. Physique* **19**, 498 (2018).
- [32] D. A. Abanin, E. Altman, I. Bloch, and M. Serbyn, Colloquium: Many-body localization, thermalization, and entanglement, *Rev. Mod. Phys.* **91**, 021001 (2019).
- [33] S. Iyer, V. Oganesyan, G. Refael, and D. A. Huse, Many-body localization in a quasiperiodic system, *Phys. Rev. B* **87**, 134202 (2013).
- [34] R. Modak and S. Mukerjee, Many-body localization in the presence of a single-particle mobility edge, *Phys. Rev. Lett.* **115**, 230401 (2015).
- [35] M. Žnidarič and M. Ljubotina, Interaction instability of localization in quasiperiodic systems, *Proceedings of the National Academy of Sciences* **115**, 4595 (2018).
- [36] S. Xu, X. Li, Y.-T. Hsu, B. Swingle, and S. Das Sarma, Butterfly effect in interacting aubry-andré model: Thermalization, slow scrambling, and many-body localization, *Phys. Rev. Res.* **1**, 032039 (2019).
- [37] N. Nesi and A. Iucci, Finite-temperature properties of one-dimensional hard-core bosons in a quasiperiodic optical lattice, *Phys. Rev. A* **84**, 063614 (2011).
- [38] N. Roy and S. Sinha, A finite temperature study of ideal quantum gases in the presence of one dimensional quasiperiodic potential, *Journal of Statistical Mechanics: Theory and Experiment* **2018**, 053106 (2018).
- [39] V. P. Michal, B. L. Altshuler, and G. V. Shlyapnikov, Delocalization of weakly interacting bosons in a 1d quasiperiodic potential, *Phys. Rev. Lett.* **113**, 045304 (2014).
- [40] S. A. Parameswaran, R. Roy, and S. L. Sondhi, Fractional quantum Hall physics in topological flat bands, *Comptes Rendus. Physique* **14**, 816 (2013).
- [41] E. J. BERGHOLTZ and Z. LIU, Topological flat band models and fractional chern insulators, *International Journal of Modern Physics B* **27**, 1330017 (2013), <https://doi.org/10.1142/S021797921330017X>.
- [42] O. Derzhko, J. Richter, and M. Maksymenko, Strongly correlated flat-band systems: The route from heisenberg spins to hubbard electrons, *International Journal of Modern Physics B* **29**, 1530007 (2015).
- [43] S. Flach, D. Leykam, J. D. Bodyfelt, P. Matthies, and A. S. Desyatnikov, Detangling flat bands into fano lattices, *Europhysics Letters* **105**, 30001 (2014).
- [44] D. Leykam, A. Andreanov, and S. F. and, Artificial flat band systems: from lattice models to experiments, *Advances in Physics: X* **3**, 1473052 (2018).
- [45] N. Roy, A. Ramachandran, and A. Sharma, Interplay of disorder and interactions in a flat-band supporting diamond chain, *Phys. Rev. Res.* **2**, 043395 (2020).
- [46] W. Maimaiti, A. Andreanov, H. C. Park, O. Gendelman, and S. Flach, Compact localized states and flat-band generators in one dimension, *Phys. Rev. B* **95**, 115135 (2017).
- [47] P. Sathe, F. Harper, and R. Roy, Compactly supported wannier functions and strictly local projectors, *Journal of Physics A: Mathematical and Theoretical* **54**, 335302 (2021).
- [48] C. Danieli, J. D. Bodyfelt, and S. Flach, Flat-band engineering of mobility edges, *Phys. Rev. B* **91**, 235134 (2015).
- [49] A. Ahmed, A. Ramachandran, I. M. Khaymovich, and A. Sharma, Flat band based multifractality in the all-band-flat diamond chain, *Phys. Rev. B* **106**, 205119 (2022).
- [50] A. Avila, Global theory of one-frequency schrödinger operators, *Acta Mathematica* **215**, 1 (2015).
- [51] Z. Wang, Y. Zhang, L. Wang, and S. Chen, Engineering mobility in quasiperiodic lattices with exact mobility edges, *Phys. Rev. B* **108**, 174202 (2023).
- [52] Y.-C. Zhang and Y.-Y. Zhang, Lyapunov exponent, mobility edges, and critical region in the generalized aubry-andré model with an unbounded quasiperiodic potential, *Phys. Rev. B* **105**, 174206 (2022).
- [53] X. Cai and Y.-C. Yu, Exact mobility edges in quasiperiodic systems without self-duality, *Journal of Physics: Condensed Matter* **35**, 035602 (2022).
- [54] Y. Wang, X. Xia, Y. Wang, Z. Zheng, and X.-J. Liu, Duality between two generalized aubry-andré models with exact mobility edges, *Phys. Rev. B* **103**, 174205 (2021).
- [55] S. Lee, A. Andreanov, and S. Flach, Critical-to-insulator transitions and fractality edges in perturbed flat bands, *Phys. Rev. B* **107**, 014204 (2023).
- [56] A. Avila, S. Jitomirskaya, and C. A. Marx, Spectral theory of extended harper's model and a question by erdős and szekeres, *Inventiones mathematicae* **210**, 283 (2017).
- [57] P. S. Davids, Lyapunov exponent and transfer-matrix spectrum of the random binary alloy, *Phys. Rev. B* **52**, 4146 (1995).
- [58] S. Jitomirskaya and W. Liu, Arithmetic spectral transitions for the maryland model, *Communications on Pure and Applied Mathematics* **70**, 1025 (2017), <https://onlinelibrary.wiley.com/doi/pdf/10.1002/cpa.21688>.
- [59] H. Weyl, Über die gleichverteilung von zahlen mod. eins, *Mathematische Annalen* **77**, 313 (1916).
- [60] G. H. Choe, Ergodicity and irrational rotations, *Proceedings of the Royal Irish Academy. Section A: Mathematical and Physical Sciences* **93A**, 193 (1993).
- [61] S. Longhi, Metal-insulator phase transition in a non-hermitian aubry-andré-harper model, *Phys. Rev. B* **100**, 125157 (2019).
- [62] I. S. Gradshteyn and I. M. Ryzhik, *Table of Integrals, Series, and Products*, seventh ed., edited by D. Zwillinger (Academic Press, Amsterdam,

- 2007).
- [63] S. Jitomirskaya and B. Simon, Operators with singular continuous spectrum: Iii. almost periodic schrödinger operators, [Communications in Mathematical Physics](#) **165**, 201 (1994).
- [64] L. F. Cugliandolo, G. Schehr, M. Tarzia, and D. Venturelli, Multifractal phase in the weighted adjacency matrices of random erdős-rényi graphs, [Phys. Rev. B](#) **110**, 174202 (2024).